Quantum delocalization of protons in the hydrogen-bond network of an enzyme active site

Lu Wang, Stephen D. Fried, Steven G. Boxer, and Thomas E. Markland[1]

Department of Chemistry, Stanford University, Stanford, CA 94305

Edited by Michael L. Klein, Temple University, Philadelphia, PA, and approved November 13, 2014 (received for review September 25, 2014)

Enzymes use protein architectures to create highly specialized structural motifs that can greatly enhance the rates of complex chemical transformations. Here, we use experiments, combined with ab initio simulations that exactly include nuclear quantum effects, to show that a triad of strongly hydrogen-bonded tyrosine residues within the active site of the enzyme ketosteroid isomerase (KSI) facilitates quantum proton delocalization. This delocalization dramatically stabilizes the deprotonation of an active-site tyrosine residue, resulting in a very large isotope effect on its acidity. When an intermediate analog is docked, it is incorporated into the hydrogen-bond network, giving rise to extended quantum proton delocalization in the active site. These results shed light on the role of nuclear quantum effects in the hydrogen-bond network that stabilizes the reactive intermediate of KSI, and the behavior of protons in biological systems containing strong hydrogen bonds.

enzyme | hydrogen bonding | nuclear quantum effects | proton delocalization | ab initio path integral molecular dynamics

Although many biological processes can be well-described with classical mechanics, there has been much interest and debate as to the role of quantum effects in biological systems ranging from photosynthetic energy transfer, to photoinduced isomerization in the vision cycle and avian magnetoreception (1). For example, nuclear quantum effects, such as tunneling and zero-point energy (ZPE), have been observed to lead to kinetic isotope effects of greater than 100 in biological proton and proton-coupled electron transfer processes (2, 3). However, the role of nuclear quantum effects in determining the ground-state thermodynamic properties of biological systems, which manifest as equilibrium isotope effects, has gained significantly less attention (4).

Ketosteroid isomerase (KSI) possesses one of the highest enzyme unimolecular rate constants and thus, is considered a paradigm of proton transfer catalysis in enzymology (5–11). The remarkable rate of KSI is intimately connected to the formation of a hydrogen-bond network in its active site (Fig. 1*A*), which acts to stabilize a charged dienolate intermediate, lowering its free energy by ∼11 kcal/mol (1 kcal = 4.18 kJ) relative to solution (Fig. S1) (6). This extended hydrogen-bond network in the active site links the substrate to Asp103 and Tyr16, with the latter further hydrogen-bonded to Tyr57 and Tyr32, which is shown in Fig. 1*A*.

The mutant KSI^{D40N} preserves the structure of the wild-type (WT) enzyme while mimicking the protonation state of residue 40 in the intermediate complex (Fig. 1*B*), therefore permitting experimental investigation of an intermediate-like state of the enzyme (6, 12–14). Experiments have identified that, in the absence of an inhibitor, one of the residues in the active site of KSI^{D40N} is deprotonated (12). Although one might expect the carboxylic acid of Asp103 to be deprotonated, the combination of recent ^{13}C NMR and ultraviolet visible spectroscopy (UV-Vis) experiments has shown that the ionization resides primarily on the hydroxyl group of Tyr57, which possesses an anomalously low pK_a of 6.3 ± 0.1 (12). Such a large tyrosine acidity is often associated with specific stabilizing electrostatic interactions (such as a metal ion or cationic residue in close proximity), which is not the case here, suggesting that an additional stabilization mechanism is at play (15).

One possible explanation is suggested by the close proximity of the oxygen (O) atoms on the side chains of the adjacent residues Tyr16 (O16) and Tyr32 (O32) to the deprotonated O on Tyr57 (O57) (Fig. 1*C*) (16). In several high-resolution crystal structures, these distances are found to be around 2.6 Å (14, 16, 17), which is much shorter than those observed in hydrogen-bonded liquids such as water, where O–O distances are typically around 2.85 Å. Such short heavy-atom distances are only slightly larger than those typically associated with low-barrier hydrogen bonds (18–20), where extensive proton sharing is expected to occur between the atoms. In addition, at these short distances, the proton's position uncertainty (de Broglie wavelength) becomes comparable with the O–O distance, indicating that nuclear quantum effects could play an important role in stabilizing the deprotonated residue (Fig. 1*C*). In this work, we show how nuclear quantum effects determine the properties of protons in the active-site hydrogen-bond network of KSI^{D40N} in the absence and presence of an intermediate analog by combining ab initio path integral simulations and isotope effect experiments.

Isotope Substitution Experiments Reveal Large Isotope Effect on Acidity

To assess the impact of nuclear quantum effects on the anomalous acidity of Tyr57, we measured the isotope effect on the acid dissociation constant on substituting hydrogens (H) in the hydrogen-bond network with deuterium (D). Because tyrosinate absorbs light at 300 nm more intensely than tyrosine, titration curves were generated by recording UV spectra of KSI^{D40N} at different *pL* values (where *L* is H or D) (15). These experiments

Significance

Because of the low mass of the proton, nuclear quantum effects can dramatically alter the properties of hydrogen-bond networks, especially when short and strong hydrogen bonds occur. Here, we combine experiments and state-of-the-art simulations that include the quantum nature of both the electrons and nuclei to show that the enzyme ketosteroid isomerase contains a hydrogen-bond network in its active site that facilitates extensive quantum proton delocalization. This leads to a 10,000-fold increase in the acidity of an active-site residue compared with the limit where the nuclei are classical particles. This work opens up new avenues for understanding the interplay between quantum effects and hydrogen bonding in biological systems containing strong hydrogen bonds.

Author contributions: L.W., S.D.F., S.G.B., and T.E.M. designed research; L.W. and S.D.F. performed research; L.W., S.D.F., S.G.B., and T.E.M. analyzed data; and L.W., S.D.F., S.G.B., and T.E.M. wrote the paper.

The authors declare no conflict of interest.

This article is a PNAS Direct Submission.

[1]To whom correspondence should be addressed. Email: tmarkland@stanford.edu.

This article contains supporting information online at www.pnas.org/lookup/suppl/doi:10.1073/pnas.1417923111/-/DCSupplemental.

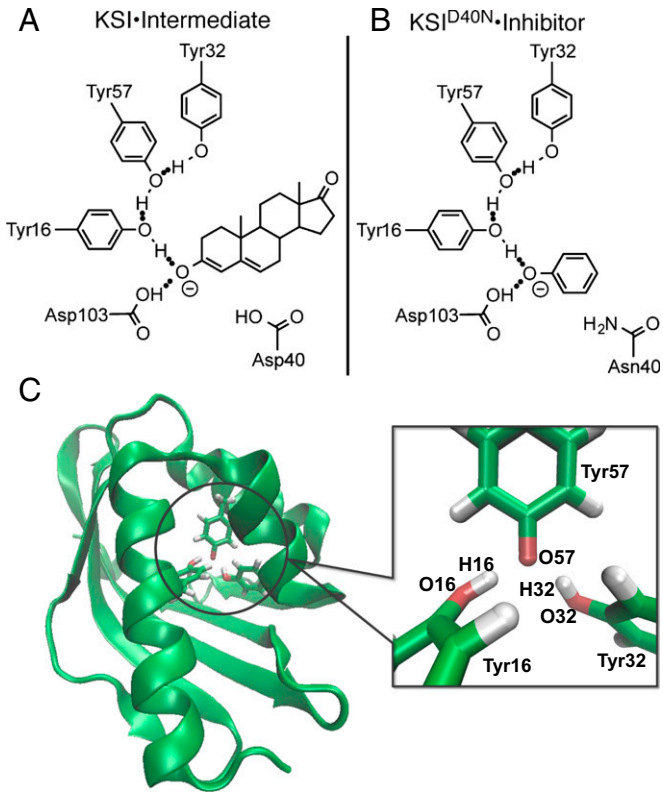

Fig. 1. KSI·intermediate and KSI^{D40N} inhibitor complex. Schematic depiction of (*A*) the KSI·intermediate complex during the catalytic cycle (Fig. S1) and (*B*) a complex between KSI^{D40N} and phenol, an inhibitor that acts as an intermediate analog. Both the intermediate and the inhibitor are stabilized by a hydrogen-bond network in the active site of KSI. (*C*) Image of KSI^{D40N} with the tyrosine triad enlarged and the atoms O16, H16, O32, H32, and O57 labeled (shown with Tyr57 deprotonated) (16).

(Fig. 2 and Table S1) reveal a change in pK_a on H/D substitution (ΔpK_a^{KSI}) of 1.1 ± 0.14 for tyrosine in the KSI^{D40N} active site. This pK_a isotope effect is much larger than that observed for tyrosine in solution ($\Delta pK_a^{Sol} = 0.53 \pm 0.08$), and it is also, to the best of our knowledge, the largest recorded pK_a isotope effect (21). Changes in static equilibrium properties, such as the pK_a, on isotope substitution arise entirely from the quantum mechanical nature of nuclei. Such a large excess isotope effect, defined as $\Delta\Delta pK_a \equiv \Delta pK_a^{KSI} - \Delta pK_a^{Sol}$, of 0.57 ± 0.16 thus indicates that the tyrosine triad in the active site of KSI^{D40N} exhibits much larger nuclear quantum effects than those observed for tyrosine in aqueous solution.

Given the possible role of nuclear quantum effects in KSI^{D40N}, can one estimate how much the quantum nature of protons changes the acidity of Tyr57 compared with a situation in which all of the nuclei in the enzyme active site were classical? In the quasiharmonic limit, one can show that the pK_a varies as the inverse square root of the particle mass (m) (22, 23). By using this relation and the experimental pL values, we can extrapolate to the classical ($m \to \infty$) limit, which yields that the pK_a of Tyr57 in KSI^{D40N} would be 10.1 ± 0.5 if the hydrogens were classical particles (Fig. S2). Relative to the observed pK_a of 6.3 ± 0.1, this value implies that nuclear quantum effects lower the pK_a of Tyr57 by 3.8 ± 0.5 units: an almost four orders of magnitude change in the acid dissociation constant.

Ab Initio Path Integral Simulations of KSI^{D40N}

To provide insights into the molecular origins of the nuclear and electronic quantum effects that stabilize the deprotonated Tyr57 residue, we performed simulations of KSI^{D40N}. To treat the electronic structure in the active site, we performed ab initio molecular dynamics (AIMD) simulations using a quantum mechanical/molecular mechanical (QM/MM) approach (24–27), in which the QM region was treated by density functional theory at the B3LYP-D3 level (28, 29) (*Materials and Methods*). These simulations allow for bond breakage and formation as dictated by the instantaneous electronic structure rather than predefined bonding rules.

AIMD simulations are typically performed treating the nuclei as classical particles. However, a classical treatment of the nuclei would predict that the pK_a would not change on isotope substitution. Nuclear quantum effects can be exactly included in the static equilibrium properties for a given description of the electronic structure using the path integral formalism of quantum mechanics, which exploits the exact mapping of a system of quantum mechanical particles onto a classical system of ring polymers (30–33). We combined this formalism with on-the-fly electronic structure calculations and performed ab initio path integral molecular dynamics (AI-PIMD) simulations of KSI^{D40N}. These simulations treat both the nuclear and electronic degrees of freedom quantum mechanically in the active-site QM region and also incorporate the fluctuations of the protein and solvent environment in the MM region. The simulations consisted of between 47 and 68 QM atoms and more than 52,000 MM atoms describing the rest of the protein and solvent (Table S2). These simulations, which until recently would have been computationally prohibitive, were made possible by accelerating the path integral molecular dynamics convergence using a generalized Langevin equation (34), using new methods to accelerate the extraction of isotope effects (22), and exploiting graphical processing units (GPUs) to perform efficient electronic structure theory evaluations through an interface to the TeraChem code (35, 36). Such a combination yielded almost three orders of magnitude speedup compared with existing AI-PIMD approaches, allowing 1.1 ps/day simulation to be obtained using six NVIDIA Titan GPUs. We have recently shown that AI-PIMD simulations using the B3LYP-D3 functional give excellent predictions of

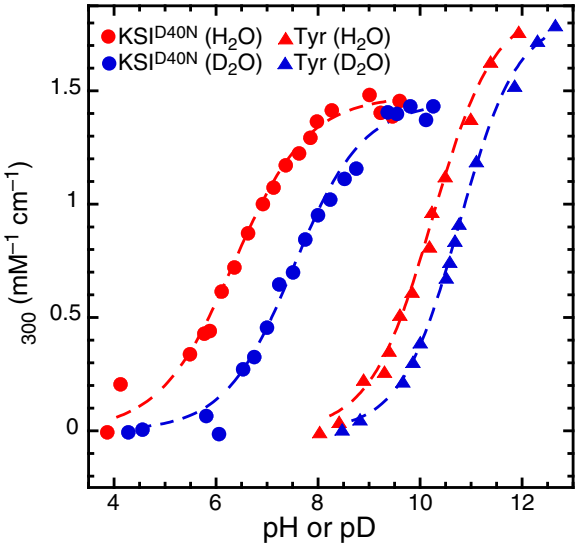

Fig. 2. Experimental UV-Vis titration curves of KSI^{D40N} (circles) and tyrosine (triangles) in buffered H_2O (red) and D_2O (blue). Fractional ionization of the phenolic moiety is monitored by measuring the change in absorption at 300 nm. All datasets were well-fit to a sigmoid function, admitting four pK_a values and two ΔpK_a values (the acidity isotope effect).

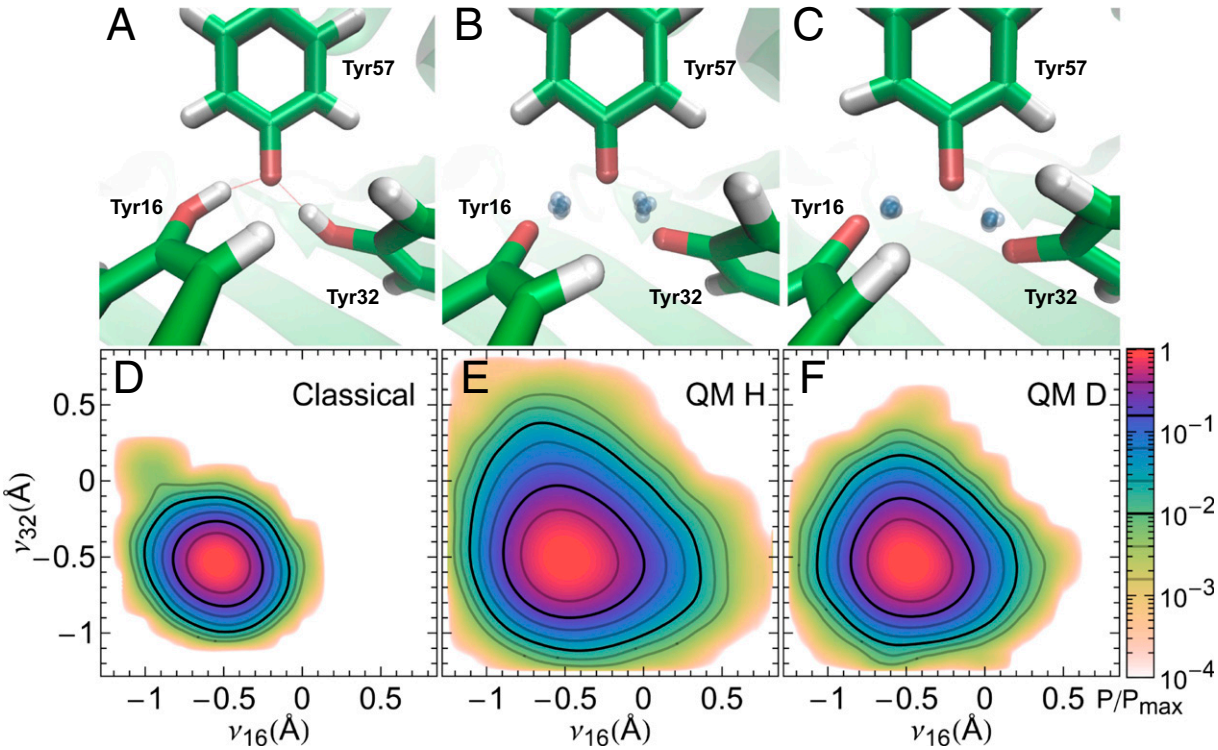

Fig. 3. Delocalized protons in the active site of KSI^{D40N} from AIMD and AI-PIMD simulations. Snapshots of (*A–C*) the active site of KSI^{D40N} and (*D–F*) probability distribution along the proton-sharing coordinates ν_{16} and ν_{32} when the nuclei are treated classically (Classical) or quantum mechanically for H (QM H) and D (QM D). In *A–C*, green, red, and white represent C, O, and H atoms, respectively. The blue-gray spheres in the QM snapshots show uncertainty in the delocalized protons positions. For clarity, all other particles are represented by their centroids. In *D–F*, probabilities are shown on a log scale and normalized by their maximum values.

isotope effects in water, validating such a combination for the simulation of isotope effects in hydrogen-bonded systems (37).

Quantum Delocalization of Protons in KSI^{D40N}

The excess isotope effect, $\Delta\Delta pK_a$, obtained from our simulations (*SI Materials and Methods*, section C) was 0.50 ± 0.03, which is in excellent agreement with the experimental value of 0.57 ± 0.16. The average distances between O57 and the adjacent O16 and O32 atoms obtained in our simulations were 2.56 and 2.57 Å, with standard deviations in both cases of 0.09 Å. The distribution of distances between O16 and O57 explored in the simulation is shown in Fig. 4*A*, *Inset*. These average O–O distances are slightly smaller than (and within the margin of error of) those in the starting crystal structure (~2.6 Å) (16). As we will discuss below, the close proximity of the neighboring O16 and O32 groups plays a crucial role in the origins of the observed isotope effect.

Fig. 3 *A–C* shows snapshots from AIMD simulations, in which the nuclei are treated classically (Fig. 3*A*) or quantum mechanically using the path integral formalism (AI-PIMD) (Fig. 3 *B* and *C*), whereas Movies S1–S3 show the simulation trajectories. For the quantum simulations, the H16 and H32 protons are shown as their full ring polymers, which arise from the path integral quantum mechanics formalism. The spread of the ring polymer representing each proton is related to its de Broglie wavelength (quantum mechanical position uncertainty) (38, 39). The uncertainty principle dictates that localization of a quantum mechanical particle increases its quantum kinetic energy. The protons will thus attempt to delocalize (i.e., spread their ring polymers) to reduce this energetic penalty. The resulting proton positions in Fig. 3*B* arise from the interplay between the chemical environment, such as the covalent O–H bond, which acts to localize the proton and the quantum kinetic energy penalty that must be paid to confine a quantum particle. Inclusion of nuclear quantum effects, thus, allows the protons to delocalize between the hydroxyl oxygens to mitigate the quantum kinetic energy penalty (Fig. 3*B*), which is not observed classically (Fig. 3*A*). Confinement of D, which because of its larger mass has a smaller position uncertainty, leads to a much less severe quantum kinetic energy penalty and hence less delocalization (Fig. 3*C*).

To characterize the degree of proton delocalization, we define a proton-sharing coordinate $\nu_X = d_{OX,HX} - d_{O57,HX}$, where $d_{OX,HX}$ is the distance of proton HX from oxygen atom OX, and $X = 16$ or 32. Hence, $\nu_X = 0$ corresponds to a proton that is equidistant between the oxygen atoms of TyrX and Tyr57, whereas a positive value indicates proton transfer to Tyr57 from TyrX. Fig. 3 *D–F* show the probability distribution along the proton-sharing coordinates ν_{16} and ν_{32} for classical and quantum nuclei for H and D, respectively. The free energies along ν_{16} and ν_{32} are provided in Fig. S3. In the classical AIMD simulation, H16 and H32 remain bound to their respective oxygens throughout the simulation (ν_{16} and ν_{32} are negative), with Tyr57 ionized 99.96% of the time (Fig. 3*D*). However, on including nuclear quantum effects (AI-PIMD simulations), there is a dramatic increase in the range of values that ν_{16} and ν_{32} can explore (Fig. 3*E*). In particular, the probability that Tyr57 is protonated ($\nu_X > 0$) increases by about 150-fold for H after including quantum effects (Fig. 3*E*), with the proton hole equally shifted onto the adjacent Tyr16 or Tyr32 residues. Proton transfers between the residues are observed frequently (Movies S2 and S3), with site lifetimes on the order of 60 and 200 fs in the H and D simulations, respectively. Although path integral molecular dynamics simulations exactly include nuclear quantum effects for calculating static properties, they do not allow rigorous extraction of time-dependent properties; nevertheless, they offer a crude way to assess the timescale of the

proton motion. The frequent transfers observed are also consistent with Fig. 3 *E* and *F*, which shows a monotonic decrease in the probability along both ν_{16} and ν_{32} [i.e., although the proton-transferred state is lower in probability, the proton-transfer process along each of the proton-sharing coordinates contains no free-energy barrier (Fig. S3) and thus, is kinetically fast].

As an experimental counterpart, we used chemical shifts of $^{13}C_{\zeta}$-Tyr–labeled KSI^{D40N} as a measure of fractional ionization of each Tyr residue (*SI Materials and Methods*, section B and Fig. S4) (14). This analysis yielded values of 79% for the Tyr57 ionization for H and 86% for D (Table S3) compared with simulated values of 94.2% and 98.3% (±0.3%), respectively. This comparison represents good quantitative agreement, because the population difference amounts to a difference in the relative free energy between experiment and theory of 0.7 kcal/mol—an error that is within the expected accuracy of the electronic structure approach used. In addition, the change in the ionization of Tyr57 obtained experimentally on exchanging H for D (7%) is in good agreement with the value predicted from our simulations (4.1%). The underprediction of the isotope effect on fractional ionization from our simulations is in line with the slightly low value of the simulated excess isotope effect, which is consistent with recent observations that the B3LYP-D3 density functional slightly underestimates the degree of proton sharing and hence, isotope effects in hydrogen-bonded systems after including nuclear quantum effects (37).

The large degree of proton sharing with the deprotonated Tyr57 residue upon including nuclear quantum effects can be elucidated by considering the potential energy required, $\Delta E_{\nu=0}$, to move a proton in the KSI tyrosine triad from its energetic minimum to a perfectly shared position between the two tyrosine groups ($\nu = 0$). $\Delta E_{\nu=0}$ depends strongly on the positions of the residues comprising the triad and in particular, the separation between the proton donor and acceptor oxygen atoms. Fig. 4*A* shows $\Delta E_{\nu=0}$ computed as a function of the distance between O16 and O57, R_{OO}, for the tyrosine triad in the absence of the protein environment. Removing the protein environment allows us to examine how changes in the triad distances from their positions in the enzyme affect the proton delocalization behavior without introducing steric overlaps with other active-site residues (*SI Materials and Methods*, section D).

Fig. 4*A* shows that, for the range of oxygen distances observed in the tyrosine triad (R_{OO} = 2.50–2.65 Å), $\Delta E_{\nu=0}$ for H16 is 3–6 kcal/mol. This energy is 6–12 times the thermal energy (k_BT) available at 300 K, leading to a very low thermal probability of the proton-shared state (lower than $e^{-6} = 2 \times 10^{-3}$). However, upon including nuclear quantum effects, the system possesses ZPE, which in this system is ∼4 kcal/mol. The ZPE closely matches $\Delta E_{\nu=0}$ and thus floods the potential energy wells along the proton-sharing coordinate (Fig. 4*B*), allowing facile proton sharing (Fig. 3) (i.e., inducing a transition to a low-barrier hydrogen bond-type regime where the protons are quantum mechanically delocalized between the hydrogen-bonded heavy atoms) (18–20). This energy match leads to qualitatively different behavior of the protons in the active site of KSI^{D40N}: from classical hydrogen bonding to quantum delocalization. The proton delocalization between the residues allows for ionization to be shared among three tyrosines to stabilize the deprotonation of Tyr57, leading to the large observed pK_a shift relative to the value in the classical limit (Fig. S2). This change in proton behavior gives rise to the large excess isotope effect, because an O–D stretch possesses a ZPE of ∼3 kcal/mol, which is no longer sufficient to fully flood the potential energy well in the proton-sharing coordinate ν. As the O–O separation is decreased below the values observed in the tyrosine triad of KSI, $\Delta E_{\nu=0}$ becomes negligible compared with the thermal energy (∼0.6 kcal/mol at 300 K). Hence, at very short distances (<2.3 Å), thermal fluctuations alone permit extensive proton sharing between the residues, and the ZPE plays

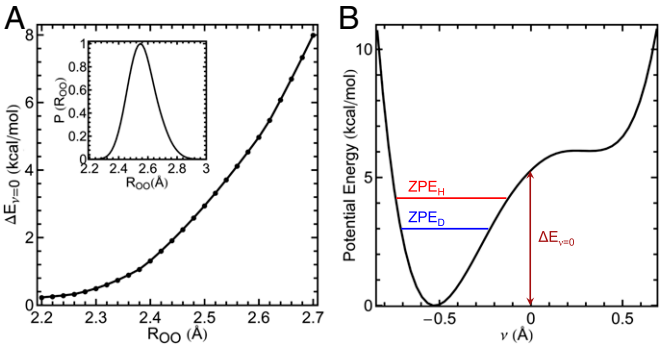

Fig. 4. Comparison of the energy required to share a proton between residues ($\Delta E_{\nu=0}$) as a function of the hydrogen-bond donor–acceptor O–O distance (R_{OO}) compared with the ZPE. (*A*) $\Delta E_{\nu=0}$ as a function of the O–O distance (R_{OO}) between O16 and O57 using the tyrosine triad geometry from a crystal structure (details in *SI Materials and Methods*, section D). *A*, *Inset* shows the probability distribution of R_{OO} obtained from the AI-PIMD simulation of KSI^{D40N} with ionized Tyr57. The probability is normalized by the maximum value. (*B*) Potential energy as a function of the proton transfer coordinate ν for R_{OO} = 2.6 Å, indicating values for H and D (O–H and O–D) ZPEs (ZPE_H and ZPE_D, respectively). The position of Tyr32 is fixed as the proton H16 is scanned along R_{OO}.

a negligible role in determining the protons positions. Thus, one would expect a small isotope effect. However, at bond lengths in excess of 2.7 Å, $\Delta E_{\nu=0}$ becomes so large (>8 kcal/mol) (Fig. 4*A*) that the ZPE is not sufficient to flood the barriers, also resulting in a small expected isotope effect (40). The large excess isotope effect in KSI^{D40N}, thus, arises from the close matching of the ZPE and the depth of the energetic well ($\Delta E_{\nu=0}$), which is highly sensitive to the O–O distance. Hence, although proton delocalization can occur classically at short O–O distances (<2.3 Å), nuclear quantum effects allow this to occur for a much wider range of O–O distances (up to ∼2.6 Å), making delocalization feasible without incurring the steep steric costs that would be associated with bringing oxygen atoms any closer. The distances in the active-site triad motif of KSI, thus, maximize quantum proton delocalization, which acts to stabilize the deprotonated residue.

Quantum Delocalization Stabilizes an Intermediate Analog by Sharing Ionization

Finally, we considered the role of nuclear quantum effects when an intermediate analog participates in the active-site hydrogen-bond network. Recent experiments have investigated how the binding of intermediate analogs to KSI^{D40N} affects the sharing of ionization along the extended hydrogen-bond network that is formed (Fig. 1*B*) (14). These experiments identified that ionization sharing is maximized when phenol, whose solution pK_a of 10 equals that of the actual intermediate of KSI (Fig. 1*A*), is bound (14, 41, 42). We thus performed AI-PIMD simulations of the KSI^{D40N}·phenol complex. The protons were observed to be delocalized across the network (Fig. 5), with partial ionizations of Tyr57, Tyr16, and phenol calculated to be 18.5%, 56.7%, and 22.5% (±0.7%), compared with estimates from previous experiments using ^{13}C NMR of 40%, 40%, and 20% (14). Hence, simulation and experiment are in good agreement that the ionization is shared almost equally among the three residues [i.e., that there is almost no difference (<2 k_BT) in the free energy after shifting the ionization among any of the three groups]. Therefore, the ability of the protons to delocalize within the KSI^{D40N} tyrosine triad, initially found in the enzyme in the absence of the intermediate analog and manifested as a strongly perturbed pK_a, extends on incorporation of the intermediate analog, which shifts the center of the ionization along the network from Tyr57 to Tyr16. In both cases, proton delocalization

CHEMISTRY

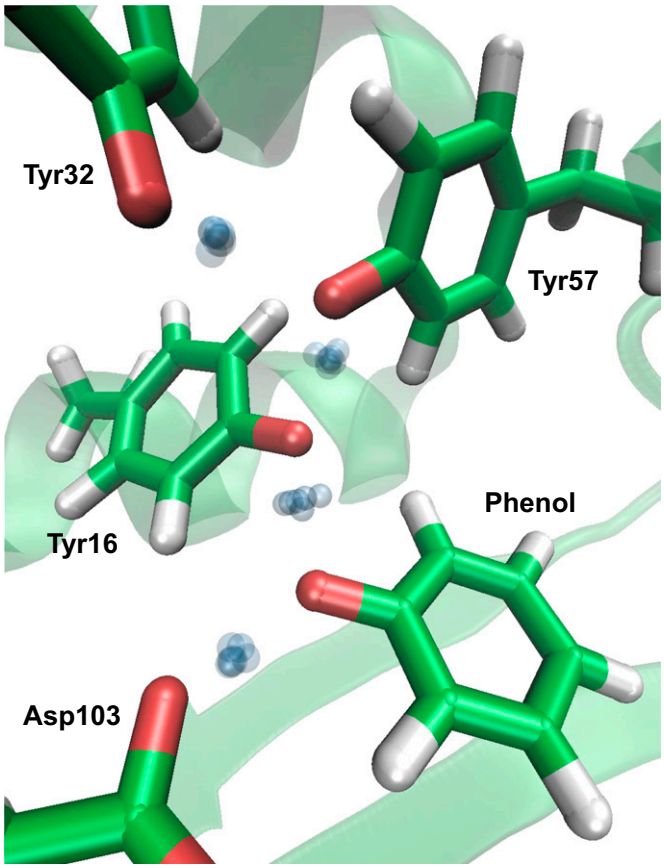

Fig. 5. Simulation snapshot of the KSI^{D40N} active site with the bound intermediate analog (phenol) that gives rise to an extended delocalized proton network. Green, red, and white represent C, O, and H atoms, respectively. The blue spheres represent uncertainty in the delocalized proton position in the hydrogen-bond network. For clarity, all other particles are represented by their centroids.

acts to share the ionization of a negatively charged group, which suggests that KSI could use quantum delocalization in its active-site hydrogen-bond network to distribute the ionization arising in its intermediate complex (Fig. 1*A*) to provide energetic stabilization.

Conclusion

In conclusion, KSI^{D40N} exhibits a large equilibrium isotope effect in the acidity of its active-site tyrosine residues arising from a highly specialized triad motif consisting of several short O–O distances, whose positions that enhance quantum delocalization of protons within the active-site hydrogen-bond network. This delocalization manifests in a very large isotope effect and substantial acidity shift. Our simulations, which include electronic quantum effects and exactly treat the quantum nature of the nuclei, show qualitatively and quantitatively different proton behavior compared with conventional simulations in which the nuclei are treated classically, and provide good agreement with experiment. The ability to perform such simulations thus offers the opportunity to investigate in unprecedented detail the plethora of systems in which short-strong hydrogen bonds occur, where incorporating both nuclear and electronic quantum effects is crucial to understand their functions.

Materials and Methods

Expression and Purification of KSI. WT and KSI^{D40N} from *Pseudomonas* putida were overexpressed in BL-21 A1 cells (Invitrogen), isolated by affinity chromatography using a custom-designed deoxycholate-bound column resin, and purified by gel filtration chromatography (GE Healthcare) as described previously (43). For ^{13}C NMR experiments, $^{13}C_{\zeta}$-tyrosine was incorporated into KSI according to the methods described previously (14).

UV-Vis Titration Experiments. A series of buffers was prepared with a *pL* between 4 and 10 by weighing portions of a weak acid and its sodium-conjugate base salt and adding the appropriate form of distilled deionized water [Millipore H_2O and Spectra stable isotopes sterile-filtered D_2O (>99% ^{2}H)]. Buffers were prepared at 40 mM. Tyr57 is solvent-accessible, and therefore, the tyrosine residues in the active-site network are expected to be fully deuterated in D_2O solution.

The following buffer systems were used for the following *pL* ranges: acetic acid/sodium acetate, 4–5.25; sodium monobasic phosphate/dibasic phosphate, 5.5–8.25; and sodium bicarbonate/sodium carbonate, 8.5–10. Buffers were stored at room temperature with caps firmly sealed.

After preparation of buffers, *pL* was recorded using an Orion2 Star glass electrode (Thermo) immediately after calibration with standard buffers at pH 4, pH 7, and pH 10. In H_2O, the pH of the buffer was taken as the reading on the electrode. In D_2O, the *pD* of the buffer was calculated by adding 0.41 to the operational pH* from the electrode reading (44). A series of samples for titration was prepared by combining 60 μL protein (100 μM stock in buffer-free L_2O), buffer (150 μL 40 mM stock), and extra L_2O. The final samples were 600 μL, 10 μM protein, and 10 mM buffer.

UV-Vis measurements were carried out on the samples on a Lambda 25 Spectrophotometer (Perkin-Elmer) that acquired data from 400 to 200 nm with a 1.0-nm data interval, a 960-nm/min scan rate, and a 1.00-nm slit width. For each measurement, a background was taken to the pure buffer of a given *pL* before acquiring on the protein-containing sample. Spectra were recorded in duplicate to control for random detector error.

The spectra were baselined by setting the absorption at 320 nm to zero, and the change in absorption at 300 nm was followed at varying *pL* values using a previously established method (15) to determine the fractional ionization of a tyrosine–tyrosinate pair. The error in A_{300} from comparing duplicate spectra after baselining was generally between 0% and 2%. For each *pL*, the average A_{300} was calculated and converted to an extinction coefficient (ϵ_{300}). The titration experiment was repeated on two independently prepared buffer stocks to control for error in buffer preparation.

Simulations. AI-PIMD and AIMD simulations were performed using a QM/MM approach of KSI^{D40N} with Tyr57 protonated, KSI^{D40N} with Tyr57 ionized, KSI^{D40N} with the intermediate analog bound, and tyrosine in aqueous solution. The simulations were carried out in the NVT ensemble at 300 K with a time step of 0.5 fs. The path integral-generalized Langevin equation approach was used, which allowed results within the statistical error bars to be obtained using only six path integral beads to represent each particle (34). The electronic structure in the QM region (Fig. S5) was evaluated using the B3LYP functional (28) with dispersion corrections (29). The 6–31G* basis set was used, because we found it to produce proton transfer potential energy profiles with a mean absolute error of less than 0.4 kcal/mol compared to using larger basis sets for this system (Fig. S6). Energies and forces in the QM region and the electrostatic interactions between the QM and MM regions were obtained using an MPI interface to the GPU-accelerated TeraChem package (35, 36). Atoms in the MM region were described using the AMBER03 force field (45) and the TIP3P water model (46). The simulations were performed using periodic boundary conditions with Ewald summation to treat long-range electrostatic interactions. The energies and forces within the MM region and the Lennard–Jones interactions between the QM and MM regions were calculated by MPI calls to the LAMMPS molecular dynamics package (47). The QM region of KSI^{D40N} contained the *p*-methylene phenol side chains of residues Tyr16, Tyr32, and Tyr57 (Fig. S5*A*). For KSI^{D40N} with the intermediate analog, residue Asp103 and the bound intermediate analog were also included in the QM region (Fig. S5*B*). The QM region of tyrosine in solution contained the side chain of the tyrosine residue and the 41 water molecules within 6.5 Å of the side-chain O–H group. All bonds across the QM/MM interface were capped with hydrogen link atoms in the QM region (26). These capping atoms were constrained to be along the bisected bonds and do not interact with the MM region.

The initial configuration of KSI^{D40N} was obtained from a crystal structure (16) (Protein Data Bank ID code 1OGX). For KSI^{D40N} with the intermediate analog, a crystal structure (14) (Protein Data Bank ID code 3VGN) was used with the ligand changed to phenol. The crystal structures were solvated in TIP3P water, and the energy was minimized before performing AI-PIMD simulations. The initial configuration for tyrosine in aqueous solution was obtained by solvating the amino acid in TIP3P (46) water using the AMBER03

force field (45) and equilibrating for 5 ns in the NPT ensemble at a temperature of 300 K and pressure of 1 bar. Each system was then equilibrated for 10 ps followed by production runs of 30 ps.

To calculate the excess isotope effect, $\Delta\Delta pK_a$ (*SI Materials and Methods*, section C), we used the thermodynamic free-energy perturbation path integral estimator (22). Combined with an appropriate choice of the integration variable to smooth the free-energy derivatives (22), this approach allowed us to evaluate the isotope effects in the liquid phase using only a single AI-PIMD trajectory. Simulations performed with D substitution showed no change within the statistical error bars reported.

ACKNOWLEDGMENTS. The authors thank Christine Isborn, Nathan Luehr, and Todd Martinez for their assistance in interfacing our program to the TeraChem code. L.W. acknowledges a postdoctoral fellowship from the Stanford Center for Molecular Analysis and Design. S.D.F. thanks the National Science Foundation (NSF) Predoctoral Fellowship Program and the Stanford Bio-X Interdisciplinary Graduate Fellowship for support. T.E.M. acknowledges support from a Terman Fellowship, an Alfred P. Sloan Research Fellowship, a Hellman Faculty Scholar Fund Fellowship, and Stanford University startup funds. This work was supported, in part, by National Institutes of Health Grant GM27738 (to S.G.B.). This work used the Extreme Science and Engineering Discovery Environment, which is supported by NSF Grant ACI-1053575 (Project TG-CHE140013).

1. Lambert N, et al. (2013) Quantum biology. *Nat Phys* 9(1):10–18.
2. Sutcliffe MJ, Scrutton NS (2002) A new conceptual framework for enzyme catalysis. Hydrogen tunnelling coupled to enzyme dynamics in flavoprotein and quinoprotein enzymes. *Eur J Biochem* 269(13):3096–3102.
3. Klinman JP, Kohen A (2013) Hydrogen tunneling links protein dynamics to enzyme catalysis. *Annu Rev Biochem* 82:471–496.
4. Pérez A, Tuckerman ME, Hjalmarson HP, von Lilienfeld OA (2010) Enol tautomers of Watson-Crick base pair models are metastable because of nuclear quantum effects. *J Am Chem Soc* 132(33):11510–11515.
5. Feierberg I, Åqvist J (2002) The catalytic power of ketosteroid isomerase investigated by computer simulation. *Biochemistry* 41(52):15728–15735.
6. Pollack RM (2004) Enzymatic mechanisms for catalysis of enolization: Ketosteroid isomerase. *Bioorg Chem* 32(5):341–353.
7. Warshel A, Sharma PK, Chu ZT, Åqvist J (2007) Electrostatic contributions to binding of transition state analogues can be very different from the corresponding contributions to catalysis: Phenolates binding to the oxyanion hole of ketosteroid isomerase. *Biochemistry* 46(6):1466–1476.
8. Chakravorty DK, Hammes-Schiffer S (2010) Impact of mutation on proton transfer reactions in ketosteroid isomerase: Insights from molecular dynamics simulations. *J Am Chem Soc* 132(21):7549–7555.
9. Hanoian P, Sigala PA, Herschlag D, Hammes-Schiffer S (2010) Hydrogen bonding in the active site of ketosteroid isomerase: Electronic inductive effects and hydrogen bond coupling. *Biochemistry* 49(48):10339–10348.
10. Herschlag D, Natarajan A (2013) Fundamental challenges in mechanistic enzymology: Progress toward understanding the rate enhancements of enzymes. *Biochemistry* 52(12):2050–2067.
11. Amyes TL, Richard JP (2013) Specificity in transition state binding: The Pauling model revisited. *Biochemistry* 52(12):2021–2035.
12. Fafarman AT, et al. (2012) Quantitative, directional measurement of electric field heterogeneity in the active site of ketosteroid isomerase. *Proc Natl Acad Sci USA* 109(6):E299–E308.
13. Fried SD, Boxer SG (2013) Thermodynamic framework for identifying free energy inventories of enzyme catalytic cycles. *Proc Natl Acad Sci USA* 110(30):12271–12276.
14. Sigala PA, et al. (2013) Quantitative dissection of hydrogen bond-mediated proton transfer in the ketosteroid isomerase active site. *Proc Natl Acad Sci USA* 110(28): E2552–E2561.
15. Schwans JP, Sunden F, Gonzalez A, Tsai Y, Herschlag D (2013) Uncovering the determinants of a highly perturbed tyrosine pKa in the active site of ketosteroid isomerase. *Biochemistry* 52(44):7840–7855.
16. Ha NC, Kim MS, Lee W, Choi KY, Oh BH (2000) Detection of large pKa perturbations of an inhibitor and a catalytic group at an enzyme active site, a mechanistic basis for catalytic power of many enzymes. *J Biol Chem* 275(52):41100–41106.
17. Sigala PA, et al. (2008) Testing geometrical discrimination within an enzyme active site: Constrained hydrogen bonding in the ketosteroid isomerase oxyanion hole. *J Am Chem Soc* 130(41):13696–13708.
18. Cleland WW, Kreevoy MM (1994) Low-barrier hydrogen bonds and enzymic catalysis. *Science* 264(5167):1887–1890.
19. Frey PA, Whitt SA, Tobin JB (1994) A low-barrier hydrogen bond in the catalytic triad of serine proteases. *Science* 264(5167):1927–1930.
20. Zhao Q, Abeygunawardana C, Talalay P, Mildvan AS (1996) NMR evidence for the participation of a low-barrier hydrogen bond in the mechanism of delta 5-3-ketosteroid isomerase. *Proc Natl Acad Sci USA* 93(16):8220–8224.
21. Wolfsberg M, Van Hook W, Paneth P, Rebelo LPN (2009) *Isotope Effects: In the Chemical, Geological, and Bio Sciences* (Springer, Dordrecht, The Netherlands).
22. Ceriotti M, Markland TE (2013) Efficient methods and practical guidelines for simulating isotope effects. *J Chem Phys* 138(1):014112.
23. Marsalek O, et al. (2014) Efficient calculation of free energy differences associated with isotopic substitution using path-integral molecular dynamics. *J Chem Theory Comput* 10(4):1440–1453.
24. Warshel A, Levitt M (1976) Theoretical studies of enzymic reactions: Dielectric, electrostatic and steric stabilization of the carbonium ion in the reaction of lysozyme. *J Mol Biol* 103(2):227–249.
25. Field MJ, Bash PA, Karplus M (1990) A combined quantum mechanical and molecular mechanical potential for molecular dynamics simulations. *J Comput Chem* 11(6):700–733.
26. Eurenius KP, Chatfield DC, Brooks BR, Hodoscek M (1996) Enzyme mechanisms with hybrid quantum and molecular mechanical potentials. I. Theoretical considerations. *Int J Quantum Chem* 60(6):1189–1200.
27. Monard G, Merz KM (1999) Combined quantum mechanical/molecular mechanical methodologies applied to biomolecular systems. *Acc Chem Res* 32(10):904–911.
28. Becke AD (1993) Density-functional thermochemistry. III. The role of exact exchange. *J Chem Phys* 98(7):5648–5652.
29. Grimme S, Antony J, Ehrlich S, Krieg H (2010) A consistent and accurate ab initio parameterization of density functional dispersion correction (DFT-D) for the 94 elements H-Pu. *J Chem Phys* 132(15):154104.
30. Feynman RP, Hibbs AR (1964) *Quantum Mechanics and Path Integrals* (McGraw-Hill, New York).
31. Chandler D, Wolynes PG (1981) Exploiting the isomorphism between quantum theory and classical statistical mechanics of polyatomic fluids. *J Chem Phys* 74(7):4078–4095.
32. Berne BJ, Thirumalai D (1986) On the simulation of quantum systems: Path integral methods. *Annu Rev Phys Chem* 37:401–424.
33. Marx D, Parrinello M (1996) Ab initio path integral molecular dynamics: Basic ideas. *J Chem Phys* 104(11):4077–4082.
34. Ceriotti M, Manolopoulos DE (2012) Efficient first-principles calculation of the quantum kinetic energy and momentum distribution of nuclei. *Phys Rev Lett* 109(10): 100604.
35. Ufimtsev IS, Martinez TJ (2009) Quantum chemistry on graphical processing units. 3. Analytical energy gradients, geometry optimization, and first principles molecular dynamics. *J Chem Theory Comput* 5(10):2619–2628.
36. Isborn CM, Götz AW, Clark MA, Walker RC, Martínez TJ (2012) Electronic absorption spectra from mm and ab initio QM/MM molecular dynamics: Environmental effects on the absorption spectrum of photoactive yellow protein. *J Chem Theory Comput* 8(12): 5092–5106.
37. Wang L, Ceriotti M, Markland TE (2014) Quantum fluctuations and isotope effects in ab initio descriptions of water. *J Chem Phys* 141(10):104502.
38. Parrinello M, Rahman A (1984) Study of an F center in molten KCl. *J Chem Phys* 80(2): 860–867.
39. Markland TE, Berne BJ (2012) Unraveling quantum mechanical effects in water using isotopic fractionation. *Proc Natl Acad Sci USA* 109(21):7988–7991.
40. McKenzie RH, Bekker C, Athokpam B, Ramesh SG (2014) Effect of quantum nuclear motion on hydrogen bonding. *J Chem Phys* 140(17):174508.
41. Fried SD, Boxer SG (2012) Evaluation of the energetics of the concerted acid-base mechanism in enzymatic catalysis: The case of ketosteroid isomerase. *J Phys Chem B* 116(1):690–697.
42. Childs W, Boxer SG (2010) Proton affinity of the oxyanion hole in the active site of ketosteroid isomerase. *Biochemistry* 49(12):2725–2731.
43. Kraut DA, et al. (2006) Testing electrostatic complementarity in enzyme catalysis: Hydrogen bonding in the ketosteroid isomerase oxyanion hole. *PLoS Biol* 4(4):e99.
44. Covington AK, Paabo M, Robinson RA, Bates RG (1968) Use of the glass electrode in deuterium oxide and the relation between the standardized pD (pa_D) scale and the operational pH in heavy water. *Anal Chem* 40(4):700–706.
45. Duan Y, et al. (2003) A point-charge force field for molecular mechanics simulations of proteins based on condensed-phase quantum mechanical calculations. *J Comput Chem* 24(16):1999–2012.
46. Jorgensen WWL, Chandrasekhar J, Madura JD, Impey RW, Klein ML (1983) Comparison of simple potential functions for simulating liquid water. *J Chem Phys* 79(2): 926–935.
47. Plimpton S (1995) Fast parallel algorithms for short-range molecular dynamics. *J Comput Phys* 117(1):1–19.

Supporting Information

Wang et al. 10.1073/pnas.1417923111

SI Materials and Methods

A. ^{13}C NMR Experiments. KSI^{D40N} labeled with $^{13}C_{\zeta}$-tyrosine was concentrated to ~1 mM in 40 mM potassium phosphate buffer (pH 7.2) and loaded into a Shigemi tube. NMR spectra were acquired at 25 °C on a 500-MHz (proton frequency) Varian INOVA spectrometer. 1D free induction decays were acquired with proton decoupling and 2-s recycle delays, processed with a 10-Hz line-broadening function, and referenced against the upfield carbon peak of sodium 3-trimethylsilyl-propionate-2,2,3,3-d_4 (0 ppm), similar to previous reports (1, 2). For spectra in H_2O, the buffer consisted of a small portion of D_2O as lock solvent (5%, vol/vol). For the D_2O samples, the solvent was 100% (vol/vol) D_2O. The ^{13}C NMR spectra are shown in Fig. S4.

B. Estimates of the Fractional Ionizations from ^{13}C NMR. Previous work has shown that the ^{13}C chemical shift of the ζ-carbon of tyrosine (analogously, C-1 of phenol) is sensitive to the ionization state of the adjacent hydroxyl group (3), shifting 10.8 ppm downfield on transitioning from a fully protonated (pH 2; 155.5 ppm) to a fully ionized (pH 14; 166.3 ppm) form. Based on these observations, we have used the chemical shifts of the assigned $^{13}C_{\zeta}$ peaks (1) to estimate the fractional ionizations ($\%I$) of the three tyrosines in the triad. The conversion between chemical shift and fractional ionization is achieved using the equation

$$\%I_{raw} = \left(\delta_{apo} - \delta_{ref}\right) / \left(166 - \delta_{ref}\right), \qquad \textbf{[S1]}$$

in which δ_{apo} is the chemical shift of one of the tyrosines (either Tyr16, Tyr32, or Tyr57) in Fig. S4*A* (Table S3), δ_{ref} is the chemical shift of the same tyrosine in a reference system in which the tyrosines are fully protonated (2), and 166 ppm is an estimate for the chemical shift of a fully ionized tyrosine. Eq. **S1** assumes a linear relationship between fractional ionization and chemical shift over the full dynamic range, which implies fast proton transfer on the NMR chemical shift timescale. This assumption seems to be valid in previous work (2, 4) and is additionally supported by the simulations presented here. Eq. **S1** also makes a more drastic assumption that changes in chemical shift can be fully attributed to changes in fractional ionization—that is, it neglects the dependence of the chemical shift on the local environment and the isotopic composition of the molecule. We, therefore, must regard the values of fractional ionization that are derived to be estimates, although both of these assumptions find some validity by comparing data found on KSI^{D40N} (Fig. S4*A*) with those of WT KSI (Fig. S4*B*) vide infra.

The fractional ionizations that arise from applying Eq. **S1** ($\%I_{raw}$) do not sum to unity (Table S3). The origin of this feature is likely because of the contribution of the KSI active-site environment, which could make the basis chemical shift for fully ionized TyrX different from that of tyrosine in solution (166 ppm). Importantly, however, the sum of the raw fractional ionizations is quite similar for the two isotopomers, suggesting that the environment effects are constant between the two isotopomers and therefore, would cancel when we calculate the change in fractional ionization on isotopic replacement ($\Delta\%I$).

We normalized the fractional ionizations by treating them with a uniform arithmetic correction:

$$\%I_{norm} = \%I_{raw} - \left(\Sigma\%I_{raw} - 100\right)/3, \qquad \textbf{[S2]}$$

which assumes that each of the three tyrosines would have the same chemical shift if it were fully ionized. This assumption is at least supported by the observation that three tyrosines have relatively similar chemical shifts when they are fully neutral, such as in WT KSI (Fig. S4*B*). Nevertheless, we caution that, because this normalization scheme is not perfect, the values reported for $\Delta\%I$ are more reliable that the absolute $\%I$ values.

The structure of WT KSI is nearly identical to that of KSI^{D40N} (including the environment around the tyrosine cluster), but in WT KSI, none of the tyrosines are ionized. On isotopic replacement, all of the resonances shift upfield by 120 ± 15 ppb, likely reflecting the intrinsic effect of isotopic composition on chemical shift. However, the shifts on isotopic replacement in KSI^{D40N} are substantially more varied and larger, suggesting that the majority of this effect cannot be merely caused by the isotopic composition itself but rather, the changes in fractional ionization that accompany it.

C. $\Delta\Delta pK_a$ Calculations. The pK_a change on H/D substitution (ΔpK_a) for KSI and tyrosine in aqueous solution can be calculated from the free-energy changes (ΔA):

$$\Delta pK_a^{KSI} = pK_a^{KSID} - pK_a^{KSIH} = \frac{\Delta A_2 - \Delta A_1}{2.303 k_B T} = \frac{\Delta A_{KSIH} - \Delta A_{KSI-} - \Delta A_H}{2.303 k_B T}$$

and

$$\Delta pK_a^{Sol} = pK_a^{TyrD} - pK_a^{TyrH} = \frac{\Delta A_4 - \Delta A_3}{2.303 k_B T} = \frac{\Delta A_{TyrH} - \Delta A_H}{2.303 k_B T}$$

for the following thermodynamic cycles:

$$\begin{array}{ccccccc}
\mathrm{KSIH} & \rightleftharpoons & \mathrm{KSI^-} & + & \mathrm{H^+} & \Delta A_1 \\
\Delta A_{KSIH}\uparrow & & \uparrow\Delta A_{KSI-} & & \uparrow\Delta A_H & \\
\mathrm{KSID} & \rightleftharpoons & \mathrm{KSID^-} & + & \mathrm{D^+} & \Delta A_2 \\
\mathrm{TyrH} & \rightleftharpoons & \mathrm{Tyr^-} & + & \mathrm{H^+} & \Delta A_3 \\
\Delta A_{TyrH}\uparrow & & & & \uparrow\Delta A_H & \\
\mathrm{TyrD} & \rightleftharpoons & \mathrm{Tyr^-} & + & \mathrm{D^+} & \Delta A_4.
\end{array}$$

Here, KSIH and KSI$^-$ denote KSI^{D40N} with the side-chain phenol group of Tyr57 neutral or ionized, respectively. KSID represents KSI^{D40N} with a neutral Tyr57 and H16, H32, and H57 replaced by D. Likewise, KSID$^-$ has an ionized Tyr57, with H16 and H32 being substituted by D. Tyr$^-$ represents tyrosine in aqueous solution with the side-chain group ionized. TyrD denotes tyrosine in aqueous solution with the side-chain O–H group being replaced by O–D.

We calculated the excess isotope effects on the pK_a ($\Delta\Delta pK_a$), which is a probe of the quantum effects caused by the enzyme environment that is not present in aqueous solution. In addition, because $\Delta\Delta pK_a$ naturally cancels the solvent contribution to ΔpK_a (see the above cycle), it significantly reduces the computational cost.

From the thermodynamic cycles, $\Delta\Delta pK_a$ is

$$\Delta\Delta pK_a \equiv \Delta pK_a^{KSI} - \Delta pK_a^{Sol} = \frac{\Delta A_{KSIH} - \Delta A_{KSI-} - \Delta A_{TyrH}}{2.303 k_B T}.$$

In the above equation, the ΔA values are free-energy changes upon converting D to H in a given system i and can be calculated

from the quantum kinetic energies of the hydrogen isotopes by (5, 6)

$$\Delta A_i = -\int_{m_D}^{m_H} d\mu \frac{\langle K_i(\mu)\rangle}{\mu}.$$

$K_i(\mu)$ is the quantum kinetic energy of a hydrogen isotope of mass μ. The quantum kinetic energy of H can be calculated directly from AI-PIMD simulations using the centroid virial estimator (7, 8), and $K_i(\mu)$ was obtained using the thermodynamic free-energy perturbation path integral estimator (5). Simulations of KSID$^-$ and KSID were performed, and the resulting $K_i(m_D)$ values were within the error bars of those obtained from the thermodynamic free-energy perturbation estimator.

D. Model Tyrosine Triad Calculations of Proton-Sharing Energy, $\Delta E_{\nu=0}$. To investigate the effect of the O–O distance between O16 and O57 on the energy required to share a proton between residues ($\Delta E_{\nu=0}$), we constructed a model of the tyrosine triad where we could systematically change the O–O distance. This model consisted of the *p*-methylene phenol side chains of residues Tyr16, Tyr32, and Tyr57, with the side chain of Tyr57 ionized. The heavy-atom positions of the tyrosine triad were taken from the Protein Data Bank ID code 1OGX (9) crystal structure of KSI^{D40N}. Because the crystal structure does not contain hydrogen atom information, hydrogen atoms were added, and their positions were optimized by energy minimization at the B3LYP-D3 level. The termini of the side chains were capped with hydrogen atoms. The resulting atoms included in the triad were, thus, identical to the QM region in the AI-PIMD simulations of KSI^{D40N} with ionized Tyr57 (Fig. S5*A*). However, in contrast to our AI-PIMD simulations, the protein environment was not included in these model calculations. Removal of the protein environment allowed us to move the tyrosine residues relative to each other to obtain values for $\Delta E_{\nu=0}$ at different O–O distances without creating overlaps with the rest of the protein.

To obtain $\Delta E_{\nu=0}$ as a function of the O57–O16 distance, Tyr32 and Tyr57 were fixed in space, and Tyr16 was translated along the O57–O16 vector. At each O–O distance, a proton scan was carried out by calculating the potential energy associated with moving the proton along the O57–O16 vector with all other coordinates held fixed. $\Delta E_{\nu=0}$ was obtained by taking the difference between potential energy at $\nu = 0$ and the lowest value of the energy obtained along the scan.

The electronic structure calculations were performed using the B3LYP functional (10) with D3 dispersion corrections (11) and the 6–31G* basis set using the TeraChem software (12).

1. Schwans JP, Sunden F, Gonzalez A, Tsai Y, Herschlag D (2013) Uncovering the determinants of a highly perturbed tyrosine pK_a in the active site of ketosteroid isomerase. *Biochemistry* 52(44):7840–7855.
2. Sigala PA, et al. (2013) Quantitative dissection of hydrogen bond-mediated proton transfer in the ketosteroid isomerase active site. *Proc Natl Acad Sci USA* 110(28): E2552–E2561.
3. Fafarman AT, et al. (2012) Quantitative, directional measurement of electric field heterogeneity in the active site of ketosteroid isomerase. *Proc Natl Acad Sci USA* 109(6):E299–E308.
4. Fried SD, Boxer SG (2012) Evaluation of the energetics of the concerted acid-base mechanism in enzymatic catalysis: The case of ketosteroid isomerase. *J Phys Chem B* 116(1):690–697.
5. Ceriotti M, Markland TE (2013) Efficient methods and practical guidelines for simulating isotope effects. *J Chem Phys* 138(1):014112.
6. Wang L, Ceriotti M, Markland TE (2014) Quantum fluctuations and isotope effects in ab initio descriptions of water. *J Chem Phys* 141(10):104502.
7. Cao J, Berne BJ (1989) On energy estimators in path integral Monte Carlo simulations: Dependence of accuracy on algorithm. *J Chem Phys* 91(10):6359–6366.
8. Herman MF, Bruskin EJ, Berne BJ (1982) On path integral Monte Carlo simulations. *J Chem Phys* 76(10):5150–5155.
9. Ha N-C, Kim M-S, Lee W, Choi KY, Oh B-H (2000) Detection of large pK_a perturbations of an inhibitor and a catalytic group at an enzyme active site, a mechanistic basis for catalytic power of many enzymes. *J Biol Chem* 275(52):41100–41106.
10. Becke AD (1993) Density-functional thermochemistry. III. The role of exact exchange. *J Chem Phys* 98(7):5648–5652.
11. Grimme S, Antony J, Ehrlich S, Krieg H (2010) A consistent and accurate ab initio parameterization of density functional dispersion correction (DFT-D) for the 94 elements H-Pu. *J Chem Phys* 132(15):154104.
12. Ufimtsev IS, Martinez TJ (2009) Quantum chemistry on graphical processing units. 3. Analytical energy gradients, geometry optimization, and first principles molecular dynamics. *J Chem Theory Comput* 5(10):2619–2628.

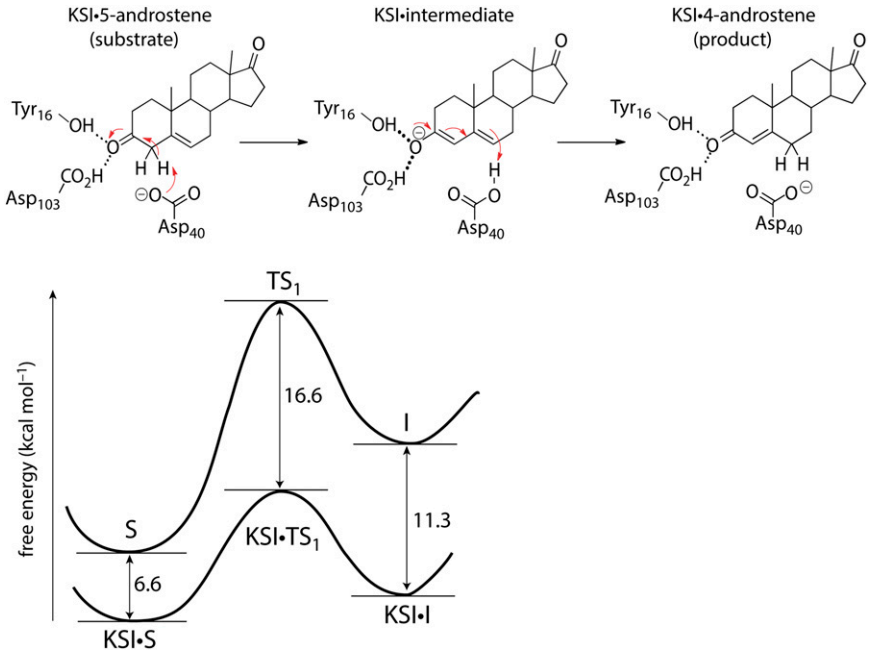

Fig. S1. Consensus mechanism of KSI. KSI rapidly converts 5-androstene to 4-androstene in two steps. The α-proton adjacent to the carbonyl is abstracted using the Asp40 general base to form an enzyme-bound dienolate intermediate. The intermediate is stabilized by 11.3 kcal/mol by accepting two direct hydrogen bonds from Tyr16 and Asp103. The proton on Asp40 is returned to the steroid two carbons away to form a conjugated ketone product. The reaction profile diagram illustrates the relative energetics between the above chemical reaction when it is catalyzed by (lower trace) KSI or (upper trace) acetate in solution. Stabilization of substrate and intermediate is based on binding constants; stabilization of the transition state (TS) is based on the ratio of rate constants.

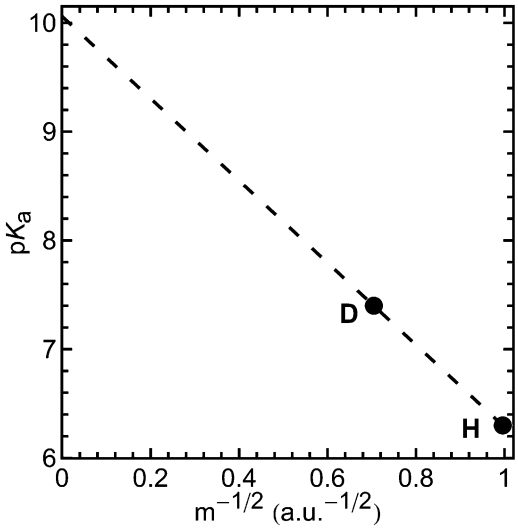

Fig. S2. Extrapolation of pK_a to classical limit. Experimental pK_a values of Tyr57 in H_2O and D_2O are shown as black dots. In the quasiharmonic limit, pK_a scales linearly with respect to the inverse square root of the hydrogen isotope mass (dotted line). The masses are in atomic units. The extrapolation to the classical limit ($m \rightarrow \infty$) yields a pK_a value of 10.1 $\pm$ 0.5 for Tyr57.

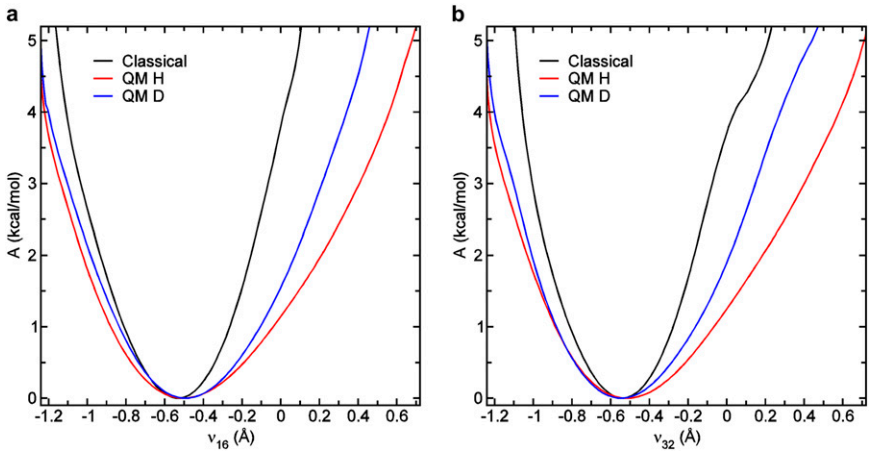

Fig. S3. Free-energy surface along the proton transfer coordinate ν. Free energy A as a function of the proton transfer coordinates (A) ν_{16} and (B) ν_{32} when the nuclei are treated classically (Classical) or quantum mechanically for H (QM H) and D (QM D).

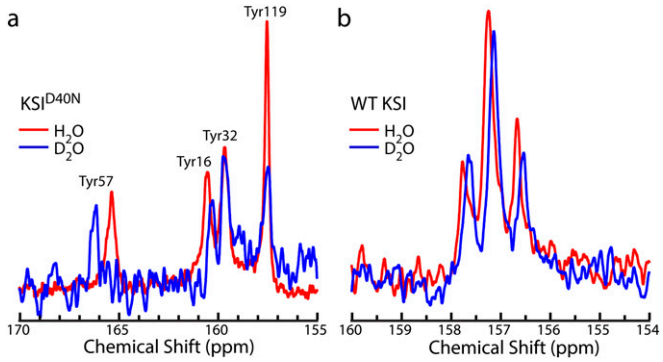

Fig. S4. Chemical shift isotope effects. ^{13}C NMR spectra of $^{13}C_\varepsilon$-Tyr–labeled KSI (A) with and (B) without the Asp40Asn mutation. Traces in red are in H_2O (5% D_2O for locking), and traces in blue are in 100% D_2O. Assignments of the peaks are shown for KSI^{D40N}. Table S3 shows fractional ionizations.

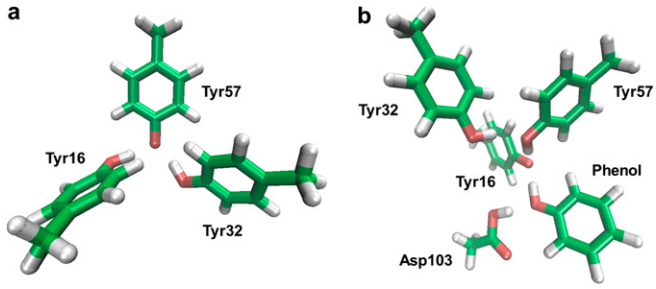

Fig. S5. QM regions used in simulations. Snapshot of the QM regions of (A) KSI^{D40N} with ionized Tyr57 (shown in the orientation in Fig. 3) and (B) KSI^{D40N} with the bound phenol (shown in the orientation in Fig. 5). Hydrogen capping atoms are also shown. Green, red, and white represent C, O, and H atoms, respectively.

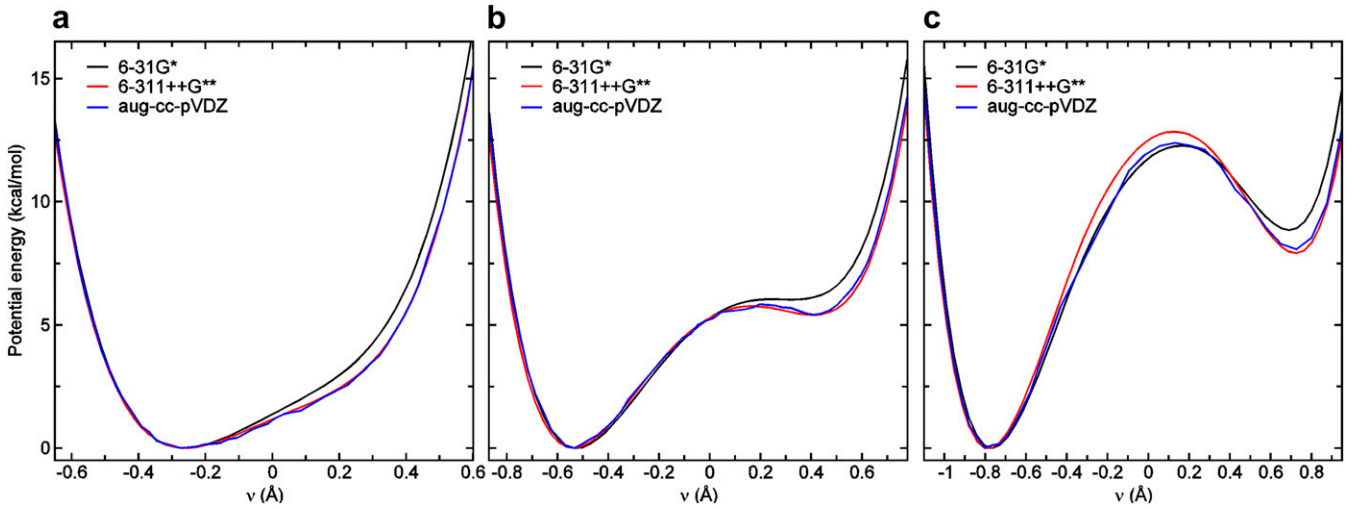

Fig. S6. Potential energy profiles showing basis set convergence. Potential energy as a function of the proton transfer coordinate ν for O–O distances of (*A*) 2.4, (*B*) 2.6, and (*C*) 2.8 Å. The electronic structure calculations were performed on the model tyrosine triad (*SI Materials and Methods*, section D) using the B3LYP functional (1) with the D3 correction (2) and the 6–31G*, 6–311++G**, and aug-cc-pVDZ basis sets. The 6–31G* basis set reproduces the potential energy profiles of the large basis sets with a maximum error of 0.9 kcal/mol and a mean absolute error of 0.4 kcal/mol in all thermally relevant regions.

1. Becke AD (1993) Density-functional thermochemistry. III. The role of exact exchange. *J Chem Phys* 98(7):5648–5652.
2. Grimme S, Antony J, Ehrlich S, Krieg H (2010) A consistent and accurate ab initio parameterization of density functional dispersion correction (DFT-D) for the 94 elements H-Pu. *J Chem Phys* 132(15):154104.

Table S1. Experimental acid dissociation constants of tyrosine and KSI^{D40N} as measured by monitoring changes in absorption at 300 nm as a function of *pL* (where *L* = H or D)

Species and solvent	pK_a^*	ΔpK_a	ΔΔpK_a
Tyrosine			
H_2O	10.24 ± 0.07	0.53 ± 0.08	
D_2O	10.77 ± 0.04		
KSI^{D40N}			0.57 ± 0.16
H_2O	6.3 ± 0.1	1.1 ± 0.14	
D_2O	7.4 ± 0.1		

Error bars are the random errors from multiple replicates, and they are propagated accordingly.

*Absolute pK_a values are subject to (sometimes significant) systematic error in the pH electrode, although this error will cancel when determining pK_a differences.

Table S2. Summary of the number of atoms in the QM and MM regions of the AI-PIMD simulations

Simulation	QM atoms	MM atoms
KSI^{D40N} with ionized Tyr57	47	56,504
KSI^{D40N} with neutral Tyr57	48	56,504
KSI^{D40N} with bound phenol	68	52,204
Tyrosine in aqueous solution	139	5,037

Table S3. ^{13}C NMR data and determination of fractional ionizations (%*I*)

		KSI^{D40N} (H_2O)			KSI^{D40N} (D_2O)			
Residue	Ref. (δ/ppm)	δ/ppm	%*I* (raw)	%*I* (norm)	δ/ppm	%*I* (raw)	%*I* (norm)	Δ%*I* (H→D)
Tyr16	158.54	160.52	26.5	13	160.26	23.0	8	−5
Tyr32	157.97	159.66	21.0	8	159.73	21.9	6	−2
Tyr57	157.97	165.36	92.0	79	166.13	101	86	+7
Total			139.5	100		145.9	100	

Chemical shifts extracted from 1D ^{13}C NMR spectra of KSI^{D40N}, in which only the ζ-carbon of tyrosine residues is enriched in ^{13}C. Fractional ionizations (%*I*) were determined using methods described in *SI Materials and Methods*, section B (1). The reference chemical shifts refer to the chemical shifts of a complex of KSI^{D40N} and 4-nitrophenol, in which the phenol is 100% ionized and the tyrosines are believed to be 0% ionized.

1. Sigala PA, et al. (2013) Quantitative dissection of hydrogen bond-mediated proton transfer in the ketosteroid isomerase active site. *Proc Natl Acad Sci USA* 110(28):E2552–E2561.

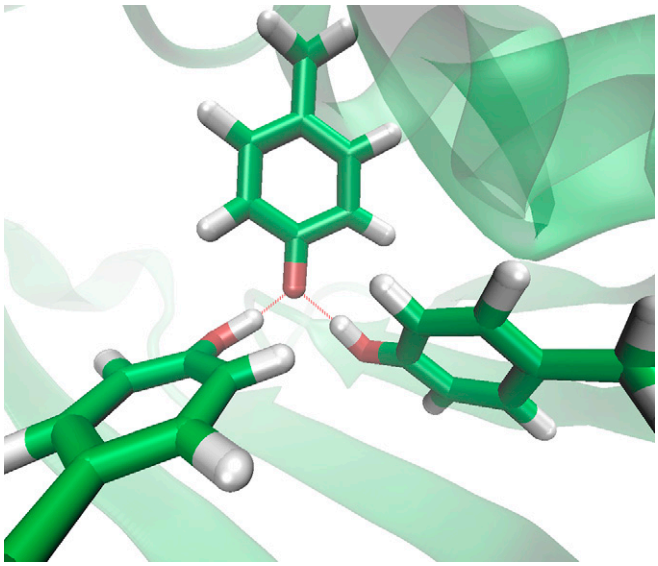

Movie S1. Trajectory of KSI^{D40N} with ionized Tyr57 from the classical AIMD simulation. H16 and H32 remain bonded to their respective oxygens throughout the simulation. Green, red, and white represent carbon, oxygen, and hydrogen atoms, respectively. The three residues shown are (*Left*) Tyr16, (*Right*) Tyr32, and (*Upper*) Tyr57. The protein environment in the MM region is also included.

Movie S1

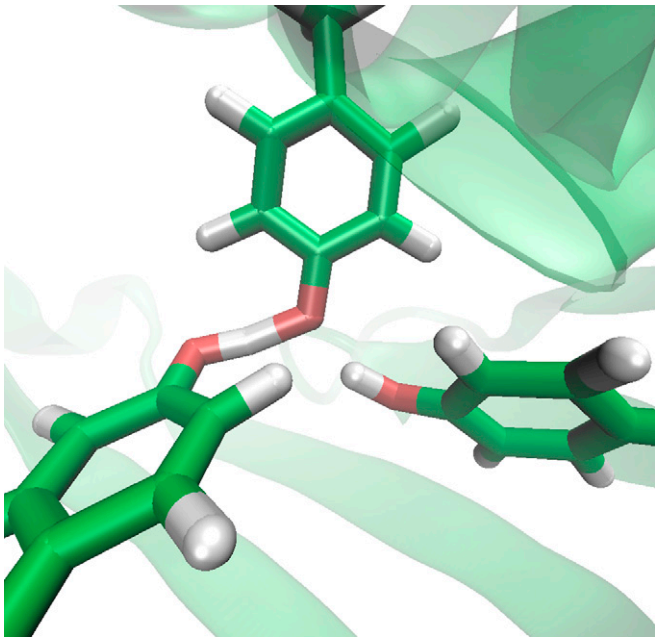

Movie S2. Trajectory of KSI^{D40N} with ionized Tyr57 from the AI-PIMD simulation. Because the six path integral beads used in the simulation are equivalent, the trajectory is shown for one bead. Frequent proton transfer can be observed in the trajectory. Green, red, and white represent carbon, oxygen, and hydrogen atoms, respectively. The three residues shown are (*Left*) Tyr16, (*Right*) Tyr32, and (*Upper*) Tyr57. The protein environment is also included.

Movie S2

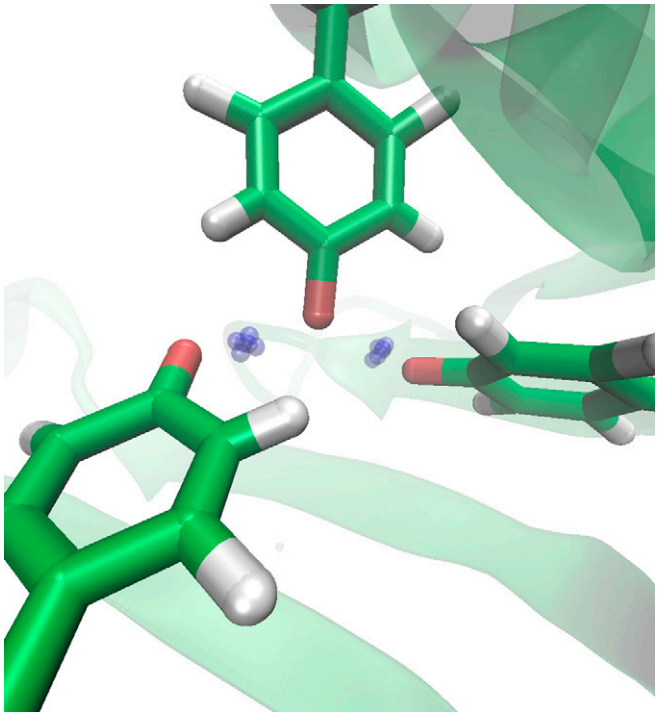

Movie S3. Trajectory of KSI^{D40N} with ionized Tyr57 from the AI-PIMD simulation. Protons H16 and H32 (shown as their full ring polymers) are delocalized between the hydrogen-bonded oxygens. Green, red, and white represent carbon, oxygen, and hydrogen atoms, respectively. The blue-gray circles represent position uncertainty of H16 and H32. For clarity, other atoms are shown as their centroids. The three residues shown are (*Left*) Tyr16, (*Right*) Tyr32, and (*Upper*) Tyr57. The protein environment is also included in the video.

Movie S3